Neutron radioscopy: industrial and scientific applications

M.A. Hickner[a], D.S. Hussey[b]

[a] Department of Materials Science and Engineering, The Pennsylvania State University, University Park, PA 16802, USA.

[b]National Institute of Standards and Technology, Gaithersburg, Maryland 20899-8461, USA.

Abstract

Neutron imaging has been a unique, precise, measurement tool for water transport in proton exchange membrane fuel cells (PEMFCs), enabling the direct measurement of the water distribution in standard, commercially viable fuel cell hardware. Thus, in the last five to seven years, neutron imaging has proven to be an invaluable tool in fuel cell research and has provided information which is inaccessible by any other measurement technique. The unique aspects of imaging real fuel cells are due to the large neutron scattering cross-section from hydrogenous liquids, combined with the relatively small scattering cross-section from many common metals and other materials of construction. Neutron imaging instruments are simple in design, and high resolution digital neutron imaging detectors (down to 20 μm) are routinely available at many neutron imaging facilities. The one drawback of neutron imaging is that a high flux neutron beamline is required, of which only six to ten facilities in the world are currently equipped to do these

types of measurements. The majority of this article discusses the uses of neutron imaging to investigate many water transport phenomena in PEMFCs, including optimal channel design, effects of thermal gradients, and material property effects on liquid water retention. In addition, examples are given of neutron tomography applied to the study of other hydrogen-based energy storage systems – metal hydride storage beds and alkaline batteries.

1 Introduction

A frequent problem in energy systems is the transport of light elements (hydrogenous liquids, lithium ions) in a metallic matrix. Measuring or visualizing this transport with traditional methods, such as x-ray scattering, magnetic resonance imaging (MRI), or optical microscopy, often results in undesirable changes to the construction of the system hardware or the methods lack sufficient sensitivity to provide accurate results. In the case of x-rays, the sensitivity increases with electron density and studying hydrogenous or lithiated materials in a metallic matrix is a measurement challenge. For optical methods, hardware modifications often include replacing the metallic or conducting components with transparent plastics, which do not have the same thermal properties. For MRI, having a metallic matrix shields the radio-frequency signal, which requires the use of specialized hardware and strong magnetic fields, greater than 10 T. However, neutrons are able to penetrate deeply through many common metals (the 1/e length for Aluminum is about 10 cm), and have a high sensitivity to light elements (the 1/e length for water is about 0.3 cm). The large attenuation by light elements is owing to the fact that neutrons interact predominately with the nuclei in a material, rather than the electron

density, as in the case of x-rays. A demonstration of light element sensitivity in the presence of metals is shown Figure 1, where a pair of Asiatic lilies inside a lead cask with a 2.5 cm wall thickness was imaged using neutrons.

This sensitivity to hydrogenous materials has been used with great success to measure water transport phenomena in proton exchange membrane fuel cells (PEMFCs). PEMFCs are an attractive energy conversion device, as the operation of PEMFCs is intrinsically clean and quiet, resulting in only electricity, waste heat, and water. By stacking several planar PEMFCs, one can manufacture an electricity generator with a power output of 100 kW or more in a form factor that readily fits inside a standard automobile. Thus, there is much interest in PEMFCs as a potential replacement to the internal combustion engine. One of the key challenges in developing PEMFCs is balancing the water content of the cell – too much water results in poor reactant flow, too little water results in poor proton conduction and resistive losses in the cell, and hence lower power. In addition, the presence of water has also been linked to component degradation. Thus, efficient water management is a key hurdle to high efficiency, long-lasting PEMFCs. Water management research spans studies of fundamental water transport in the proton exchange membrane and porous media, to the applied engineering of flow channel and gas manifold design. As discussed in Section 3, this range of topics has been investigated with neutron radiography in conjunction with other methods.

This article will discuss the basics of a neutron imaging, including a typical beam line layout, common detector systems and a discussion of neutron imaging techniques –

radiography, tomography, and phase imaging – in Section 2. An overview of fuel cell operation and a discussion of the neutron imaging experiments that have been performed to elucidate the water transport behavior in PEMFCs will be given in Section 3. Other applications of neutron tomography to energy storage system – metal hydride beds and alkaline batteries – will be given in Section 4.

2 Neutron Imaging Instrumentation and Methods

2.1 Neutron Imaging Facility Conceptual Design

Neutron imaging instruments are conceptually simple physical layouts. A fission reactor or spallation source produces high energy (several MeV) neutrons. These energetic neutrons inelastically scatter from a hydrogenous moderating medium, and come to thermal equilibrium with the moderator. The moderated neutron source has a spectrum of energies described by a Maxwellian distribution, and the temperature of the moderator is the characteristic temperature of the distribution. For neutron imaging, there are two primary temperature (and hence energy) regimes, referred to as thermal (neutron kinetic energy of 25 meV from a moderator temperature of 323 K) and cold (neutron kinetic energy of 5 meV from a moderator temperature of about 20 K).[1] For a neutron imaging beam, neutrons diffuse away from the moderator and are collimated by a pinhole aperture, with characteristic dimension D (D~1 mm to 20 mm), some distance from the

source. The aperture forms a pinhole image of the neutron source at the detector position, a distance L (L~3 m to 15 m) from the aperture. A sample is placed close to the detector, with a separation z, with z « L. The geometry of the imaging beamline is the ultimate limit to the image spatial resolution, called the geometric blur, λ_g, which from similar triangles is given by: $\lambda_g = \frac{D\,z}{L - z} \approx z\,\frac{D}{L}$. (1)

The neutron intensity at the detector scales as $(D/L)^2$. Thus reducing λ_g by decreasing D or increasing L by a factor of 2 results in a factor of 4 reduction in neutron intensity and thus longer image acquisition times. For imaging experiments where one dimension is more critical than others, such as the through-plane water content in PEMFCs, a rectangular slit can be used. The narrow dimension of the slit is aligned with the through-plane direction of the cell, while the wide dimension of the slit is aligned with the in-plane direction, thereby optimizing the spatial resolution requirements and maintaining a high neutron intensity at the detector position. The other means to reduce λ_g is to minimize the sample dimension along the neutron beam path. For PEMFC research, this means minimizing the active area width, and placing gas line and electrical connections upstream from the detector so that the test section can be mounted flush to the detector face.

2.2 Neutron Imaging Detectors

Neutron imaging has benefited greatly from recent advances in detector technology, both from light sensors such as charged-coupled devices and microchannel plates (MCPs). As both technologies continue to advance, it is anticipated the spatial resolution of neutron

images will be limited by the flux of the neutron source rather than by detector technology. The current state-of-the-art detector spatial resolution is about 0.02 mm, and is expected to be improved to about 0.01 mm in the near future with next generation MCP technology.[2,3,4] The challenge of neutron detectors is that since the neutron is an electrically neutral particle, it cannot be directly detected. Rather, a neutron is first absorbed, and the nuclear reaction yields energetic charged particles products. For imaging detectors, these charged particles are detected either through scintillation light or charge amplification in microchannel plates (MCPs). The range of charged particles before losing all kinetic energy through electromagnetic interactions in typical solids is of order 1 μm to 10 μm, and this is an estimate on the best possible spatial resolution for neutron detectors. In neutron scintillators, the light is emitted in all directions, and this further limits the spatial resolution to about the thickness of the scintillator material. A practical limit to the thickness of a scintillator is the neutron detection efficiency, as the stopping power of the scintillator is an exponential function of the scintillator thickness. A typical neutron scintillator based on ^{6}LiF doped in ZnS has about a 20 % detection efficiency for thermal neutrons at a thickness of 0.3 mm. Since cold neutrons have about a factor of 2 larger absorption cross-section, the cold neutron detection efficiency is about a factor of 2 larger than thermal neutrons. There have been recent reports on the use of thin, 10 μm, gadoxysulfide scintillators at cold neutron imaging facilities that have achieved a spatial resolution of about 20 μm.[3,4] The scintillation light is typically viewed by a digital imager, such as a charged-coupled device (CCD) through a lens and mirror at a 45 ° angle. The mirror is necessary to locate the CCD outside of the main neutron beam path to avoid radiation damage to the sensor. The advantages of a

scintillator/CCD detector system include the reasonably low equipment cost, the lens system allows the user to optimize the detector field of view and spatial resolution for the object under study, and since it is an integrating detector, there is negligible detector deadtime effects. Disadvantages of a CCD are the reduction in light collection efficiency of the lens system, and so low noise CCDs are required. An alternative to a CCD is an amorphous silicon detector. Since the sensor is amorphous, it is radiation hard and can be placed directly in the neutron beam, and thus in close contact with the neutron scintillator. The amorphous silicon detector overcomes the light collection efficiency, and enables taking images at high frame rates, up to 30 fps. However, the image spatial resolution is fixed by the pixel pitch of the detector. Current commercially available amorphous silicon detectors have a pixel pitch of about 0.125 mm, and from the Nyquist sampling theorem, this limits the spatial resolution to about 0.25 mm, which is well-matched to ^{6}Li-based scintillators.

MCP-based detectors utilize a stack of MCPs, wherein the walls of the topmost MCP are doped with a highly neutron absorbing material, such as ^{10}B or ^{nat}Gd. An energetic charged particle from the neutron capture enters an open channel of the MCP, and ejects electrons into the channel. A high negative voltage is applied across the MCP stack, which accelerates the electrons down the channel, creating a charge avalanche, similar to a photomultiplier tube, with a charge amplification of order 10^{6}. A two dimensional position sensitive anode, either a cross delay line anode or cross strip anode, measures the location of the charge cloud from arrival times of the charge pluses, which means that MCPs are event-based detectors.[5,6] The advantages of the MCP detector include a high thermal neutron detection efficiency from using a relatively thick (about 0.7 mm) neutron

sensitive MCP, negligible electronic noise, and detector spatial resolution that is at the limit of the charged particle range. Disadvantages of MCP detectors include the relatively higher sensitivity to gamma-rays compared to scintillators and there is a limit to the global event rate since MCPs are event-based with a finite deadtime to reconstruct the event position. Thus, for a fixed incident fluence rate, there is a maximum field of view.

2.3 Neutron Imaging Methods

2.3.1 Transmission Radiography and Tomography

Neutron radiography and tomography are transmission imaging techniques that have been used to extensively study mass transport. The utility of neutron techniques versus other investigative methods stems from the nature of the interaction of the neutron with matter. The neutron interaction with matter is dominated by the strong nuclear force, so that the neutron interacts primarily with the nucleus rather than the electrons in material. There are three processes that lead to neutron attenuation: absorption, incoherent spin-flip scattering, and coherent scattering. In transmission neutron imaging, only the transmitted beam in the forward direction is measured, and the three processes are described by a single collision cross-sectional area, σ_{tot}, called the total neutron scattering cross section. The unit of area is referred to as a barn (b) with 1 b = 10^{-24} cm^2. The neutron transmission through a sample is given from the Lambert-Beer law of attenuation as

$$I = I_0 \exp(- N \sigma_{tot} t), \quad (2)$$

where I is the transmitted intensity, I_0 is the incident intensity, N is the material number density and t is the sample thickness. The product $N \sigma_{tot} = \mu$ is referred to as the attenuation coefficient (or macroscopic cross-section). Typical sizes for σ_{tot} range from 10^{-24} cm^2 to 10^{-21} cm^2, so that the attenuation coefficient ranges from 10^{-2} cm^{-1} to 10 cm^{-1}. Shown in Figure 2 are the attenuation coefficients for many common materials used in proton exchange membrane fuel cells and some common battery systems over a range of incident neutron energies commonly used in transmission neutron imaging.[7] Since the interaction is dominated by the nucleus, different isotopes of the same element have different σ_{tot}. Two examples of this are hydrogen (^1H) has about a factor of 10 larger σ_{tot} than deuterium (^2H or D) and ^6Li and ^7Li, where ^6Li has a very strong neutron absorption cross section, while ^7Li has $\sigma_{tot} < 1$ b. In addition to isotope effects, σ_{tot} can depend on the incident neutron kinetic energy. For crystalline materials the transmission can be increased due to a reduction in the coherent Bragg scattering when the neutron wavelength is too long to be diffracted by a given lattice plane. This is referred to as Bragg-edge imaging, and can be used to determine crystalline composition as well as material stress. Neutron absorption is also energy dependent, as the absorption probability increases inversely proportional to the neutron velocity.[8] In addition, molecular rotational and vibrational effects can also effect σ_{tot}, as is the case with hydrogenous liquids such as water.[9]

In radiography, one typically studies an object under dynamic conditions. For instance, two-dimensional images of a fuel cell under operation during transient conditions are

acquired to resolve time-dependent correlations between water content and transient electrical performance. In this case, what is of interest is the water thickness in various regions of the fuel cell, which can be obtained from equation (2). First, a calibration experiment is performed to measure μ using known thicknesses of water. A typical method is to precisely machine steps of known and constant depths into a flat plate. A second flat plate is bolted to the face of the steps to form a seal with no gaskets. The attenuation from each step is then plotted and fitted by linear regression. It is expected that μ will vary from neutron imaging facility, since μ is generally neutron energy dependent, and each neutron imaging facility has a unique neutron energy spectrum over which the image is averaged. Once μ has been measured, one first acquires an image of the fuel cell in a completely dry state, which corresponds to I_0, and as the fuel cell operates, one collects images, I. The water thickness is then

$$t = -1/\mu \ln(I/I_0). \quad (3)$$

For measuring the in-plane water content of fuel cells (that is discriminating channel from land water) the typical water thickness is of order 0.1 mm. The typical pixel pitch for in-plane imaging experiments is about 0.125 mm, which yields a water volume of about 1.5 μL per pixel. Typical water thickness measurement uncertainties are less than 0.01 mm, or 150 nL.[10] Thus, neutron radiography is able to accurately measure, *in situ,* the locally small changes in the liquid water content typical of fuel cells. The use of neutron radiography to study water transport phenomena in PEMFCs is discussed in more detail in Section 3.

Neutron tomography is mathematically identical to x-ray computed tomography or CAT scans. Tomography is based on the Radon transform, in which a series of two-dimensional images collected at discrete angles spanning a 180 º range are viewed as a Fourier transform of the three-dimensional object. In order to reconstruct the 3-D object from the images, the filtered back projection algorithm is applied to the data, for which Hounsfield and Cormack won then Nobel Prize for Medicine in 1979. The mathematics of tomographic reconstruction are not discussed here, but the reader is referred an excellent introduction on the subject by Kak and Slaney.[11] Since tomography is a Fourier method, it is important to have a sufficient number of two-dimensional projections in order to avoid aliasing. A rule of thumb is that the angular increment, $\Delta\theta$, between each two-dimensional image should result in a motion that is less than or equal to the detector pixel pitch, or

$$\Delta\theta = 2\,\delta_p / d, \qquad (4)$$

where δ_p is the pixel pitch of the detector and d is the diameter of the object. Since multiple images of the object from different angels are required, tomography is an inherently steady-state metrology tool. There has been work to reduce the number of required projections or to ease the steady-state restrictions so as to expand the use of tomography.[12,13]

The output of the tomographic reconstruction is the local three-dimensional μ. In order to interpret the results, a calibration procedure identical to that for radiography must be performed. Since tomography requires several minutes for data acquisition, the object must be in an equilibrium state – at least on the timescale of the entire tomographic scan. But, by comparing the change in μ(x,y,z) for different equilibrium conditions, one can measure changes in concentration profiles. There have been a few reports of neutron tomography of fuel cells, but these suffered from insufficient spatial resolution to provide detailed information about the through-plane water content.[14,15,16] Tomography has been recently applied to study other energy systems, including hydrogen storage beds and battery systems, which are discussed below in Section 4.

2.3.2 Phase Imaging

Since the neutron is a massive particle, the neutron exhibits wave behavior with a wavelength given by the DeBrogile relationship, $\lambda = h/\sqrt{(2\ m\ E)}$. For cold neutrons (E = 5 meV), λ = 0.40 nm, and for thermal neutrons (E = 25 meV), λ = 0.18 nm. For imaging, this means that with a quasi-coherent source of neutrons it is possible to obtain neutron phase images.[17] In neutron phase imaging, one measures the phase shift of the neutron wave after passing through a sample. The phase shift, Δφ, is due to coherent scattering effects, and in the case of nuclear coherent scattering is given by

$$\Delta\varphi = N\ b_c\ \lambda\ t \qquad (5)$$

where b_c is the coherent scattering length, $b_c \sim 10^{-6}$ nm, and for cold neutrons, the product $b_c \lambda \sim 10^{-21}$ cm^2 to 10^{-20} cm^2, which is 2 to 3 orders of magnitude larger than σ_{tot}. This means that for equal neutron fluence rates, phase imaging is significantly more sensitive to variations in either the number density or thickness of a sample than transmission imaging. However, until recently, the quasi-coherence requirements were met by using a very small pinhole aperture, which resulted in very low neutron intensities, and hence long exposure times (of order a day). A new technique has emerged based on the Talbot effect, which requires coherence along only one dimension, enabling the use of a source grating, rather than a pinhole.[18] The grating has an open area of about 50 %, which greatly increases the neutron intensity compared to the single pinhole method. This grating approach is still rather nascent, and applications beyond proof-of-principle experiments have not been published. However, these initial experiments have shown that one can measure the dark-field image of the sample, which is related to the small angle scattering. This might allow one to measure the change in the particle size and morphology of a porous sample.

3 Neutron Imaging of Proton Exchange Membrane Fuel Cells

3.1 Background

The mechanisms of liquid water generation, buildup, and transport are some of the most highly pursued areas in applied fuel cell research. Fuel cells are electrochemical energy conversion devices that consume a fuel, in many cases hydrogen for a high-power

application such as automotive, and an oxidant, usually oxygen from the air, and convert the chemical energy directly to electrical energy with some waste heat production, The benefit of hydrogen/air fuel cells is that they only produce water, which must eventually be exhausted from the system, but this water production can be the source of major performance losses in unoptimized cells. Moreover, as proton exchange membrane fuel cell operation can span a large range of conditions with cell temperatures from -40 ºC to 120 ºC, inlet gas humidity from 0 to 100 %, and current densities from milliamps to amps per square centimeter, liquid water is ubiquitous and will occur at some point in a cell's operation.

Water is formed in fuel cells by the oxygen reduction reaction at the cathode. In the fuel cell process, air is normally fed to the cathode compartment where oxygen diffuses to the catalyst site. Protons, generated in the hydrogen oxidation reaction at the anode and transported across a proton exchange membrane, then combine with the oxygen at a catalytic site to form water. The water must be expelled from the reaction site in order to allow continued current production. As the current increases in the cell, the water production increases proportionally. Because of recent large strides in fuel cell performance over the last decade due to advanced materials, operational strategies, and fabrication technique, water management in the cell has emerged as a major mechanism of performance loss. The transport mechanisms of water away from the cathode catalyst layer are an important area of experimental and theoretical research. Because of coupled diffusion, reaction, and two-phase flow conditions in sub-micron reticulated geometries, testing model predictions and providing insightful experimental data on the water

distribution inside an operating fuel cell is still a challenge. The constrained geometry of modern fuel cell materials does not facilitate direct observation and measurement of mass and heat transport in the functional components of the fuel cell. Catalyst layers are on the order of 5 μm to 20 μm thick with pore sizes ranging from 50 nm to 1 μm. The catalyst layer is often in contact with a dense microporous layer and a macroporous substrate, which is often termed the gas diffusion layer, or GDL. These porous layers in a fuel cell are critical to achieving high performance, but they also present the reactants and products with a tortuous path to and from the catalyst site. The saturation or fraction of pore volume filled with liquid in these layers can have a dramatic effect on fuel cell performance.

Thermal gradients also play a role in the water balance of the cell. The heat produced by a fuel cell, Q_{cell}, is proportional to its operating voltage according to Equation 6,[19]

$$Q_{cell} = (V_{HHV} - V_{cell})I \tag{6}$$

where V_{cell} is the cell potential, V_{HHV} is the energy content of hydrogen based on the higher heating value (1.48 V) or enthalpic potential, and I is the total cell current. The heat generated in the reaction can be a driving force to vaporize water and to move water through other mechanisms such as thermo-osmosis.[20] The non-isothermal nature of the fuel cell is important in driving phase transitions or thermal transport away from the catalyst layer, either through the porous GDL on the cathode side, or through the membrane to the anode side of the cell.

A significant number of techniques are now available for evaluating the water content of operating fuel cells.[21] There have been many theoretical investigations of the water generation and transport in fuel cells.[22,23] The most advanced models today are able to account for two-phase flow and non-isothermal operation. Detailed depictions of the pore space in the porous media are available,[24] but most fuel cell simulations that incorporate the electrochemical reactions use an effective media or equivalent pore network model in lieu of the real geometry to describe the pore space in the catalyst and gas diffusion layers.

The development of incisive experimental tools to characterize the transport of water is an important area of fuel cell research and engineering. Optical visualization,[25] nuclear magnetic resonance imaging,[26] x-ray radiography,[27] and neutron radiography[28] have been used as direct probes for liquid water in operating cells. Optical visualization is a potentially high speed, high resolution technique which has been employed successfully to characterize the behavior of liquid water in the gas flow channels, on the surface of the GDL, and also on the surface of the catalyst layer. While optical methods are well-developed and relatively inexpensive, they can be difficult to employ where optical access is difficult to achieve, such as internal to the GDL) and. NMR imaging methods are based on the huge advances in magnetic resonance imagine (MRI) for medical and biological use. MRI scanning provides three-dimensional information without drastic changes to cell components, therefore it is a valuable tool for learning about the water balance of the cell. However, the resolution of the latest MRI of fuel cells has approached 10 μm along the through-plane direction for small, plastic cells. Imaging

large-scale fuel cells (approaching 50 cm^2) at high resolution has not been demonstrated and is not anticipated in the near future. X-ray radiography and tomography have been used successfully to look at both full-cells and small areas of operating cells. So far the cell active areas proved using x-ray methods have been limited to cells in the range of 10 cm^2 to 20 cm^2. The sub-micron resolution capability of x-ray synchrotron beam lines has been used effectively to give a microscopic view of water transport in the GDL pores and gas flow channels. Using synchrotron radiation for imaging can also result in radiation damage to the polymer membrane, and many tests are limited to an exposure time of about 30 minutes. Neutron radiography is a valuable tool for imaging liquid water in fuel cells because the attenuation of the neutron beam by liquid water is greater than the other materials of construction usually used in fuel cell hardware such as aluminum, carbon, and fluorinated polymers. Therefore, the inherent contrast of water inside the cell allows one to resolve very small amounts of liquid water. Additionally, neutron imaging systems can be built for large-area detection, allowing one to interrogate full-sized fuel cells on the order of 300 cm^2 under real-world operating conditions with minimal if any modification to the standard hardware.

3.2 Fuel Cell Neutron Imaging Basics

In order to generate a neutron radiograph of a fuel cell, there are a few key experimental precautions that must be taken. First, a dry image of the system is critical for

highlighting the regions with excess liquid water, and determining the quantitative water concentration. Dry images may be taken before or after the fuel cell experiments, but it is important to maintain the position of the cell as the normalization of the dry features must be nearly perfect (movement of the cell must be significantly less than the pixel pitch to maintain image registration for normalization). Also, it is important to avoid stray water in the cell during neutron radiography experiments. In some early experiments, the carbon plates used in many fuel cell experiments were porous in the area of the machined flow fields. This porosity caused a small amount of water contained within the carbon flow fields to vary with the cell conditions, making an accurate determination of water in the MEA impossible. Gold-coated aluminum has been found to be a suitable material for cell component construction. In addition, automotive fuel cell stacks are based on stamped stainless steel, so use of metallic flow fields is a reasonable experimental condition.

The high spatial resolution attainable with neutron imaging is ideal for investigating channel-level phenomena in operating cells. Shown in Figure 4 are neutron radiographs of a 50 cm^2 operating fuel cell, one of the standard cell designs in the community. The false color image on the right of Figure 4 showing the water thickness as a function of area is further detailed below in Figure 4 to demonstrate that both large area and high resolution (both spatial and temporal) information can be obtained with neutron radiography. By imaging the entire active area of the cell simultaneously, one may zoom-in to the areas of interest after the experiment is completed, as shown in Figure 5.

In most full-cell studies, the spatial resolution is about 100 μm to 200 μm leaving 5 pixels to 10 pixels across typical cell flow field features which are of order 1 mm.

Temporal and spatial resolution can be balanced to achieve the desired time and spatial domain information. Temporal resolution is somewhat dependent on the specific detector being employed, but image sampling on the order of 30 Hz is not unreasonable. At these high frame rates, relatively few neutrons are probing the sample under test and the signal to noise in the images is typically too low to achieve detailed spatial information. With increased single-frame acquisition time and some averaging in the data analysis, sufficient image quality can be obtained with sampling on the order of 1 Hz to 0.1 Hz. As discussed later, this type of sample frequency is sufficient to capture the change in water content due to liquid water slug advection or cell current transients.

In terms of operating conditions, fuel cells have been studied with neutron radiography over a large range of temperature, current, and relative humidity. There has been interesting work on fuel cells during freezing (below 0 ºC) conditions, high temperature fuel cells, low current operation and anode flooding, and the effect of inlet gas humidity. Clearly, neutron radiography is a versatile tool for gaining quantitative data on the liquid water distribution and concentration in fuel cell systems and may also be extended to other electrochemical applications such as direct methanol fuel cells, electrolyzers, and electro-active polymer actuators. In all of these applications, the movement of water and issues of water distribution and two-phase flow are critical to understanding both the

fundamentals of how devices operate and the engineering considerations that must be dealt with to achieve high performance.

3.3 Full-cell studies

The most useful results so far in using neutron radiography to explore fuel cell behavior has been full-cell studies where 50 cm^2 active area cells or larger can be interrogated over the entire area at once. The active region of state-of-the-art large-area amorphous silicon detectors is about 500 cm^2, therefore, automotive-class fuel cells of 300 cm^2 or larger can be imaged. These detectors also have resolution on the order of 200 μm, so they provide sufficient resolution to distinguish land/channel boundaries and corners in flow field patterns with characteristic dimensions on the order of 1 mm. Fuel cell operational conditions investigated using full-cell studies include variations in gas flow inlet location, flow field design, input humidity, cell temperature, current, and materials. Many studies have now been able to map the liquid water content of an operating cell to the cell conditions.

One counter-intuitive finding is that operation at higher current densities, where water production is at its maximum, does not always yield the most liquid water in the cell. Hickner, *et al*,[29] showed that the water content of an operating cell reaches a maximum at low to intermediate current density. Liquid water is allowed to build up in the cell at low current densities as a result of relatively low shear from the gas flow and minimal evaporation by waste heat production. As the cell current is increased, more heat is

generated, and the cell tends to become drier. The drying begins near the gas inlets where the incoming air becomes sub-saturated due to the increased local cell temperature and liquid water appears where the gases become saturated due to water production at the cathode. The strong effect of evaporation can be observed more readily as the cell temperature is raised. At 80 ºC, the inlet of the cell is much drier due to the increased evaporation caused by the local heating of the cell. The results in Figure 6 and Figure 7 illustrate the importance of considering the local temperature and heat generation of the cell when probing the two-phase flow characteristics.

Full-cell studies have allowed detailed analysis to separate the water underneath the lands and channels of the cell.[30] The authors of the study showed that as the land/channel contact ratio on the gas diffusion layer increased, the amount of stored water in the cell also increased indicating that water was stored in the cell preferentially under the land areas. While increased stored water is not advantageous under highly humidified conditions where liquid water removal can be an issue, the land/channel ratio can be tuned to combat membrane drying under low humidity operating conditions.

Channel profile designs and channel coatings have been screened using neutron radiography as a tool to probe the water content and morphology of the liquid water droplets.[31] This study illustrated that design choices can be informed by a combination of fuel cell performance and neutron radiography data. The same study observed that gas diffusion media with lower in-plane permeability caused increased liquid water accumulation within the cell.[31] Thus, for a variety of applications, neutron radiography

has been useful in adding to the data needed to both validate models and to make engineering decisions on construction materials and geometry of cell components. The possibility also exists to diagnose degradation phenomena. By correlating localized high concentrations of liquid water or areas of severe drying with post-mortem diagnoses of long-term failures, there may be value in eliminating "hot-spots" or distribution anomalies in the short term to promote long-term durability.

3.4 Microscopic imaging

The high-resolution limit of neutron imaging for fuel cells is currently 10 μm to 30 μm using microchannel plate detector technology. At the time of this publication, a 10 μm detector developed by UC Berkeley Space Sciences Laboratory is currently being tested at NIST. The first high-resolution studies were conducted with a 25 μm microchannel plate detector which limits the effective resolution of the experiment to approximately 30 μm.[2] Microscopic water gradients across the membrane electrode assembly and flow channels have been resolved as a function of current density.[32] Shown in Figure 8 is a water content profile from anode gas flow channel/gas diffusion layer interface (pixel row 0) to the cathode gas flow channel/gas diffusion layer interface (pixel row 235). These profiles span approximately 400 μm and show distinct concentrations of water in the membrane and at the gas flow channel/gas diffusion layer interfaces.

Bolliat, *et al*, have used a tilted, thin scintillator detector setup to obtain enhanced spatial resolution for imaging the water content profile across the cell.[3] When this detector was

used in conjunction with a high L/D ratio achieved with a slit aperture, full-width half-maximum edge profiles were reduced to 20 μm. With this improved-resolution detector, high concentrations of water on the cathode side of an operating cell were observed at 70 ºC and 1 A cm^{-2}. Increased local concentrations of liquid water were detected underneath the lands of the flow fields during undersaturated conditions. During saturated conditions in the cathode flow, the gas diffusion layer was saturated evenly across the land/channel contacts or even oversaturated in the channel areas.

In addition to experimentally determining the water distribution in the through-plane direction of an operating PEMFC, high-resolution experiments have been conducted to probe the transfer of liquid water across the cell, under varying thermal gradients.[33] It is anticipated that high-resolution experiments will continue to grow in importance as the detector technology and availability improves over the next several years. While the large-scale imaging of fuel cells and other devices will continue to be important, the possibilities of microscopic imaging open up entirely new investigations for model validation, materials design, and characterization of as-yet unobserved phenomena.

3.5 Time-resolved studies

The temporal resolution of neutron radiography of in-plane PEMFC water content is generally limited to about 1 Hz. Amorphous silicon detectors and many CCDs can acquire data at up to 30 Hz, but the image quality at this high frame rate tends to be low due to the low number of neutron counts and poor signal to noise statistics. With 1 Hz

imaging, much information can be gained on the changes in the cell as a function of time as the conditions are incremented. For instance, when the current density is changed, the water production, waste heat, and downstream gas humidity also change with different time scales. The electrical response of the cell in terms of voltage and current tends to be rapid. However, the water content can change slowly over periods of 10 s to 100 s of seconds. Hickner, *et al*, have investigated the coupled transient response of liquid water and the electrical response of the cell.[34] Shown in Figure 9 is the time-resolved water build-up response of a fuel cell in response to a step-change in current density from open circuit to 1.5 A cm^{-2} at 60 °C and 4 stoichiometry gas flow. At first, water fills the entire active area within the GDL. Once the GDL has reached saturation, liquid water is injected into the gas channels, and is removed from the cell through either evaporation or advection. The gas stream becomes saturated with vapor as it nears the outlet, and this is evidence by the excess liquid water near the bottom right of the cell in Figure 9.3 to 9.6. Also clear are the purges due to the increase in pressure as the liquid clogs the gas channel.

3.5 Tomography

Three-dimensional information on the distribution of liquid water through the fuel cell has long been sought. An early and still-valid criticism of the full-cell studies is that it was difficult or impossible to separate the water on the anode and cathode sides of the cell. Neutron tomography where full three-dimensional information on the liquid water

content can be obtained is a promising, yet experimentally challenging technique to execute. There have been reports of tomographic reconstructions of neutron radiographs of fuel cells, but most reports have focused on stack-level information,[14] rather than cell-level information[15,16] as discussed above. The difficulties with spatial blur, long acquisition times, and small water movements during image acquisition make neutron tomography an especially challenging technique. There are other methods for obtaining three-dimensional image data from neutron experiments such as small angle neutron scattering.[35]

3.6 Combination techniques

As neutron radiography methods have progressed and more has become known about the imaging of single cells, combination techniques are useful in supplementing the image information.

Segmented cells have been used to provide both resistance and current density information along with the water content yielded by neutron radiography. Schneider, *et al*[36] used a segmented cell in conjunction with neutron imaging and impedance to study the relationship between liquid water content and the electrical characteristics of the cell. As shown in Figure 10, they observed that the regions with moderate to significant water content had the greatest current density. Severe regions of drying and flooding were also observed in their co-flow experiments and they proved that large variations in local cell conditions can occur depending on operating parameters.

Hartnig, *et al*, observed similar results in their neutron radiography/segmented cell experiments.[37] They also observed a relatively uniform liquid water distribution across the cell active area at low currents. While there was still significant liquid water present in the channels, the current densities were low enough as to not cause mass transport limitations due to partial channel obstructions. As the current density was increased, these channel blockages caused performance decreases in the local areas in which they occurred. Also, in their counterflow arrangement, the area of maximum current density shifted towards the anode inlet at higher currents and flooding losses were observed at the outlet of the cell. Accompanying the flooding observed near the outlet of the cell was drying near the inlet of the cell similar to the observations of Schneider, *et al*.[36]

Optical and neutron imaging have been used in combination to obtain information on the total liquid water content of the cell from the neutron images, and to isolate the behavior of the water in the gas flow channels optically. The experimental setup by Prasad, *et al*, employed a neutron transparent mirror to obtain both optical and neutron images simultaneously.[38] Optical techniques have been used for some time to investigate liquid water in the gas flow channels in fuel cells, however optical methods are only useful for imaging surface water on the GDLs or water in the channels and the contrast is often low. The study by Prasad *et al* surmounts the contrast problem by analyzing images where both neutron and optical data are available. The optical images allow for separation of high concentrations of liquid water found on the anode or cathode side and can provide complimentary information on slow changes in total liquid water content of the cell from

the neutron data along with rapid liquid water droplet advection by taking advantage of the superior temporal resolution of optical imaging.

4 Neutron Tomography of Energy Storage Devices

Two examples of neutron tomography are discussed to demonstrate the use of the technique for applications other than fuel cells. The first is hydrogen uptake in a prototype hydrogen storage bed made of $LaNi_{5-x}Sn_x$,[39] the second is studying the changes in a AA alkaline cell during discharge.[40]

The metal hydride bed, described in detail in reference Bowman, *et al* (2003), consisted of a ≈90 % porous aluminum foam which was filled with metal powder.[41] The foam provided structural integrity and improved the thermal conductivity of the system. A heater rod with four turns ran the length of the bed and was in contact with the aluminum foam to heat the metal hydride in order to desorb the hydrogen. Hydrogen gas was introduced into and removed from the bed via a hollow stainless steel filter tube. Two tomograms of the hydrogen storage bed were acquired. The first was after the bed was heated to 100 °C and evacuated to a pressure below 10^{-6} mbar. The second was after the bed was filled with about 12 standard liters of hydrogen. The absorption of hydrogen by $LaNi_{5-x}Sn_x$ is exothermic. Also, hydrogen uptake is reduced at higher temperatures. Thus, colder regions will preferentially absorb hydrogen. The non-uniform distribution of hydrogen in the bed is shown clearly in Figure 11.

There have been several reports on using neutron radiography for lithium-based batteries to measure lithium ion migration and electrolyte consumption.[42] This research exploits the very large neutron absorption cross-section of ^{6}Li. In alkaline primary cell research, the neutron attenuation is dominated by the aqueous electrolyte, similar to the situation in proton exchange membrane fuel cells, as shown in Figure 2. The current spatial resolution of neutron imaging does not permit direct measurement of cathode or anode particle growth which is on the order of a few micrometers, but is more than adequate to measure the changes in the electrolyte during cell discharge. Tomograms of two AA alkaline cells were acquired before and after discharge to a cell potential of 0 V.[40] Shown in Figure 12 are tomographic slices through two different AA batteries after the end of life achieved by two different current draw conditions, 50 mA and 1 A. In the initial state, the distribution of electrolyte is homogenous in the anode and the cathode. Also, the separator, which composed of a hydrogenous material such as rayon and the porosity is filled with electrolyte solution, is clearly visible and is highly attenuating to neutrons. The distribution of the electrolyte after the cell potential has fallen to 0 V clearly depends on the discharge rate. By optimizing particle size to reduce the removal of electrolyte from the anode, it is possible to increase the cell capacity.

5 Conclusions

Neutron radiography and tomography leverages the large contrast difference between light elements to many common metals to reveal mass transport in a variety of systems of interest. The technique has been used extensively to study water transport in proton

exchange membrane fuel cells, revealing the importance of channel geometry, diffusion media material properties, and thermal gradients from anode to cathode. While no technique can yield complete information, neutron radiography and tomography have significantly advanced the fuel cell community's understanding of water distributions in operating devices. Used in combination with electrical and thermal characterization of the fuel cell, neutron imaging has provided unique insights into the coupled nature of mass and heat transport in geometrically irregular, multilayer fuel cell structures. In addition, neutron radiography and tomography have been employed to study the hydrogen uptake in a metal hydride bed, and the changes in electrolyte and ion migration in both alkaline and lithium batteries.

References

1. http://en.wikipedia.org/wiki/Thermal_neutron

2. D. S. Hussey, D. L. Jacobson, M. Arif, J. P. Owejan, J. J. Gagliardo, T. A. Trabold, "Neutron images of the through-plane water distribution of an operating PEM fuel cell," Journal of Power Sources, 172, 225-228 (2007).

3. P. Boillat, D. Kramer, B. C. Seyfang, G. Frei, E. Lehmann, G. G. Scherer, A. Wokaun, Y. Ichikawa, Y. Tasaki, K. Shinohara, "In situ observation of the water

distribution across a PEFC using high resolution neutron radiography," Electrochemistry Communications, 10, 546-550 (2008).

4. N. Kardjilov, "Emerging Techniques with Neutron Imaging", Short Course on Neutron Radiography, International Conference on Neutron Scattering, Knoxville, TN, May 3, 2009.

5. Siegmund O.H.W., Vallerga J.V., Martin A., *et al*, "A high spatial resolution event counting neutron detector using microchannel plates and cross delay line readout", Nuclear Instruments & Methods, Section A, 579 188-191, (2007).

6. Tremsin A.S., Vallerga J.V., McPhate J.B., *et al*, "On the possibility to image thermal and cold neutron with sub-15 mu m spatial resolution", Nuclear Instruments & Methods, Section A, 592, 374-384 (2008).

7. http://www.nndc.bnl.gov/exfor/exfor00.htm

8. V.F. Sears, "Neutron Optics", Oxford University Press, New York, NY, 1989.

9. Edura, Y., Morishima N., "Cold and thermal neutron scattering in liquid water: cross-section model and dynamics of water molecules", Nuclear Instruments & Methods, Section A, 534, 531-543 (2004).

10. D.S. Hussey, D.L. Jacobson, M. Arif, K.J. Coakley, and D.F. Vecchia, "In situ fuel cell water metrology at the NIST neutron imaging facility," accepted, Journal of Fuel Cell Science and Technology, 2008.

11. A.C. Kak and M. Slaney, "Principle of Computerized Tomography", Society of Industrial and Applied Mathematics, Philadelphia, PA, 2001.

12. E.J. Candès, J. Romberg, and T. Tao, "Robust Uncertainty Principles: Exact Signal Reconstruction From Highly Incomplete Frequency Information", IEEE Transactions On Information Theory, 52, 489-509 (2006).

13. D. Butnariu, R. Davidi, IEEE, G.T. Herman, and I.G. Kazantsev, "Stable Convergence Behavior Under Summable Perturbations of a Class of Projection Methods for Convex Feasibility and Optimization Problems", IEEE Journal Of Selected Topics In Signal Processing, 1, 540-547, (2007).

14. R. Satija, D. L. Jacobson, M. Arif, S. A. Werner, "In situ neutron imaging technique for evaluation of water management systems in operating PEM fuel cells," J. Power Sources, 129(2), 238-245 (2004).

15. D. S. Hussey, J. P. Owejan, D. L. Jacobson, T. A. Trabold, J. Gagliardo, D. R. Baker, D. A. Caulk, M. ARIF, “Tomographic Imaging of an Operating Proton Exchange Membrane FuelCell”, Neutron Radiography, edited by M. Arif and R.G. Downing, DEStech Publications, Inc., Lancaster, Pennsylvania, 2008.

16. I. Manke, Ch. Hartnig, N. Kardjilov, M. Grünerbel, J. Kaczerowski, A. Hilger, W. Lehnert, and J. Banhart, “Neutron Radiography and Tomography on Fuel Cells - Recent Developments at CONRAD”, Neutron Radiography, edited by M. Arif and R.G. Downing, DEStech Publications, Inc., Lancaster, Pennsylvania, 2008.

17. B. E. Allman, P. J. McMahon, K. A. Nugent, D. Paganin, D. L. Jacobson, M. Arif, and S. A. Werner, Nature, 408, 158 (2000).

18. F. Pfeiffer, C. Grünzweig, O. Bunk, G. Frei, E. Lehmann, and C. David, Physical Review Letters, 96, 215505 (2006).; H. F. Talbot "Facts relating to optical science" No. IV, Philos. Mag. 9 (1836).; Lord Rayleigh "On copying diffraction gratings and on some phenomenon connected therewith" Philos. Mag. 11 (1881).

19. J. Larminie and A. Dicks, Fuel Cells Explained, 2nd ed., John Wiley & Sons, Ltd., West Sussex, England (2003).

20. R. Zaffou, J. S. Yi, H. R. Kunz, J. M. Fenton, "Temperature-Driven Water Transport Through Membrane Electrode Assembly of Proton Exchange Membrane Fuel Cells," Electrochem. Solid-State Lett., 9(9), A418-A422 (2006).

21. J. St-Pierre, "PEMFC in situ liquid-water-content monitoring status," J. Electrochem. Soc., 154(7), B724-B731 (2007).

22. C.-Y. Wang, "Fundamental Models for Fuel Cell Engineering," Chem. Rev., 104, 4727 (2004).

23. A. Z. Weber, J. Newman, "Modeling transport in polymer-electrolyte fuel cells," Chem. Rev. 104(10), 4679-4726 (2004).

24. P. K. Sinha, P. P. Mukherjee, C. Y. Wang, "Impact of GDL structure and wettability on water management in polymer electrolyte fuel cells ," J. Meter Chem. 17(30), 3089-3103 (2007).

25. K. Tuber, D. Pocza, C. Hebling, "Visualization of water buildup in the cathode of a transparent PEM fuel cell," J. Power Sources, 124(2), 403-414 (2003).

26. K. R. Minard, V. V. Viswanathan, P. D. Majors, L.-Q. Wang, P. C. Rieke, "Magnetic resonance imaging (MRI) of PEM dehydration and gas manifold flooding during continuous fuel cell operation," J. Power Sources, 161, 856-863, (2006).

27. P. K. Sinha, P. Halleck, C.-Y. Wang, "Quantification of liquid water saturation in a PEM fuel cell diffusion medium using x-ray microtomography," Electrochem. Solid-State Lett., 9(7), A344-A348, (2006).

28. R. J. Bellows, M. Y. Lin, M. Arif, A. K. Thompson, D. Jacobson, "Neutron imaging technique for in situ measurement of water transport gradients within Nafion in polymer electrolyte fuel cells," J. Electrochem. Soc. 146(3), 1099-1103 (1999).

29. M. A. Hickner, N. P. Siegel, K. S. Chen, D. S. Hussey, D. L. Jacobson, M. Arif, "Understanding Liquid-Water Distribution and Removal Phenomena in an Operating PEMFC via Neutron Radiography," J. Electrochem. Soc., 155(3), B294-B302 (2008).

30. A. Turhan, K. Heller, J.S. Brenizer, M.M. Mench, "Passive control of liquid water storage and distribution in a PEFC through flow-field design," Journal of Power Sources, 180, 773-783 (2008).

31. J. P. Owejan, T. A. Trabold, D. L. Jacobson, M. Arif, S. G. Kandlikar, "Effects of flowfield and diffusion layer properties on water accumulation in a PEM fuel cell," International Journal of Hydrogen Energy, 32, 4489-4502 (2007).

32. M. A. Hickner, N. P. Siegel, K. S. Chen, D. S. Hussey, D. L. Jacobson, M. Arif, "In-situ High Resolution Neutron Radiography of Cross-sectional Liquid Water Profiles in Proton Exchange Membrane Fuel Cells," J. Electrochem. Soc., 155(4), B427-B434 (2008).

33. S. Kim, M. M. Mench, "Investigation of Temperature-Driven Water Transport in Polymer Electrolyte Fuel Cell: Phase-Change-Induced Flow," J. Electrochem. Soc., 156, B353 (2009).

34. M. A. Hickner, N. P. Siegel, K. S. Chen, D. S. Hussey and D. L. Jacobson, "Observations of Transient Flooding in a Proton Exchange Membrane Fuel Cell Using Time-Resolved Neutron Radiography," submitted.

35. G. Gebel, O. Diat, S. Escribano, and R. Mosdale, "Water profile determination in a running PEMFC by small-angle neutron scattering," Journal of Power Sources, 179(1), 132-139 (2008).

36. I. A. Schneider, D. Kramer, A. Wokaun, G. G. Scherer, "Spatially resolved characterization of PEFCs using simultaneously neutron radiography and locally resolved impedance spectroscopy," Electrochemistry Communications, 7, 1393-1397 (2005).

37. C. Hartnig, I. Manke, N. Kardjilov, A. Hilger, M. Grunerbel, J. Kaczerowski, J. Banhart, W. Lehnert, "Combined neutron radiography and locally resolved current density measurements of operating PEM fuel cells," Journal of Power Sources, 176, 452-459 (2008).

38. D. Spernjak, S. G. Advani, and A. K. Prasad, "Simultaneous Neutron and Optical Imaging in PEM Fuel Cells", J. Electrochem. Soc., 156(1), B109-B117 (2009).

39. D. L. Jacobson, D. S. Hussey, T. J. Udovic, J. J. Rush, R. C. Bowman, Jr., "Neutron Imaging Studies of Metal Hydride Storage Beds", submitted to Journal of Power Sources 2009.

40. D.S. Hussey, G. Riley, D.L. Jacobson, "*In Situ* Neutron Imaging of Alkaline and Lithium-ion Batteries", to be submitted to ECS Transactions 2009.

41. R.C. Bowman, Jr., M. Prina, D.S. Barber, P. Bhandari, D. Crumb, A. S. Loc, G. Morgante, J.W. Reiter, and M.E. Schmelzel, "Evaluation of Hydride Compressor Elements for the Planck Sorption Cryocooler", Cryocoolers **12** 627–635 (2003).

42. M. Kamata, T. Esaka, K. Takami, S. Takai, S. Fujine, K. Yoneda, K. Kanda, "Studies on the lithium ion conduction in Ca0.95Li0.10W0, using cold neutron radiography", Solid State Ionics **91**, 303-306 (1996).; M. Lanz, E. Lehmann, R. Imhof, I. Exnar, P. Novak, "In situ neutron radiography of lithium-ion batteries during charge/discharge cycling", Journal of Power Sources, **101**, 177-181 (2001).; N. Kardjilov, A. Hilger, I. Manke, M. Strobla, W. Treimer, J. Banhart, "Industrial applications at the newcold neutron radiography and tomography facility of the HMI", NIM A **542,** 16–21, (2005).

Figure 1: On the left is a photograph taken from the top of the of a lead cask of two Asiatic lilies. On the right is a neutron radiograph of the lilies taken from the side. Thermal neutrons easily penetrate the 2.5 cm thick lead walls, and yet demonstrate high sensitivity to the fine details in the leaves and can resolve the structure of the interior of the bloom – an impossible task for x-ray radiography.

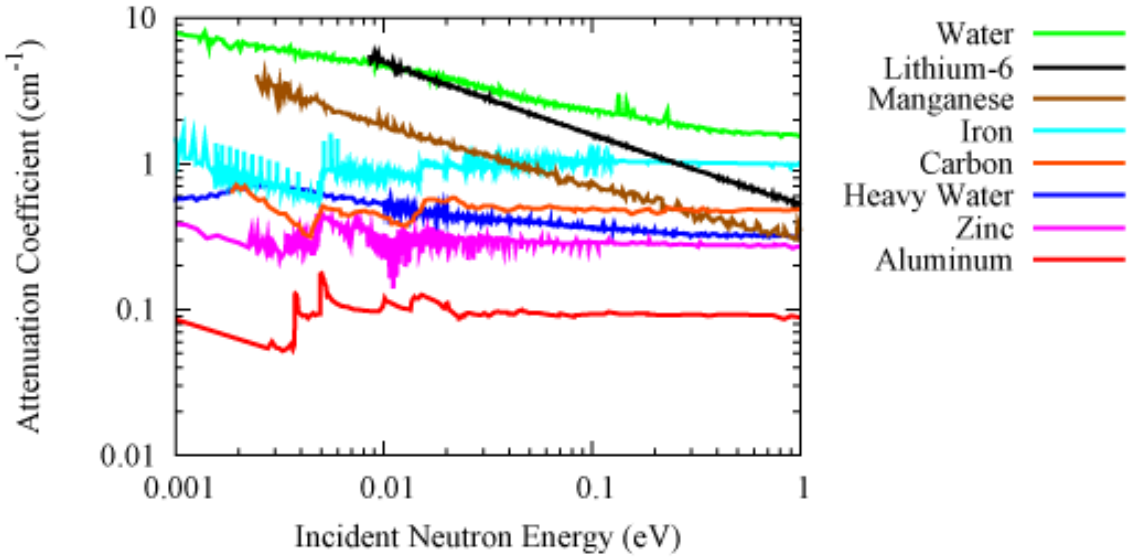

Figure 2: Neutron attenuation coefficients as a function of incident neutron energy covering the cold, thermal, and epithermal energy regimes. The attenuation coefficients are the product of the number density at room temperature and the measured total neutron scattering cross section. The total scattering cross sections are available from the Experimental Nuclear Reaction Data (EXFOR / CSISRS) database. The peaks in the zinc, manganese, and aluminum attenuation coefficients are due to neutron Bragg scattering from the crystalline structure. The attenuation coefficient for carbon is that of amorphous carbon, and hence does not manifest Bragg scattering.

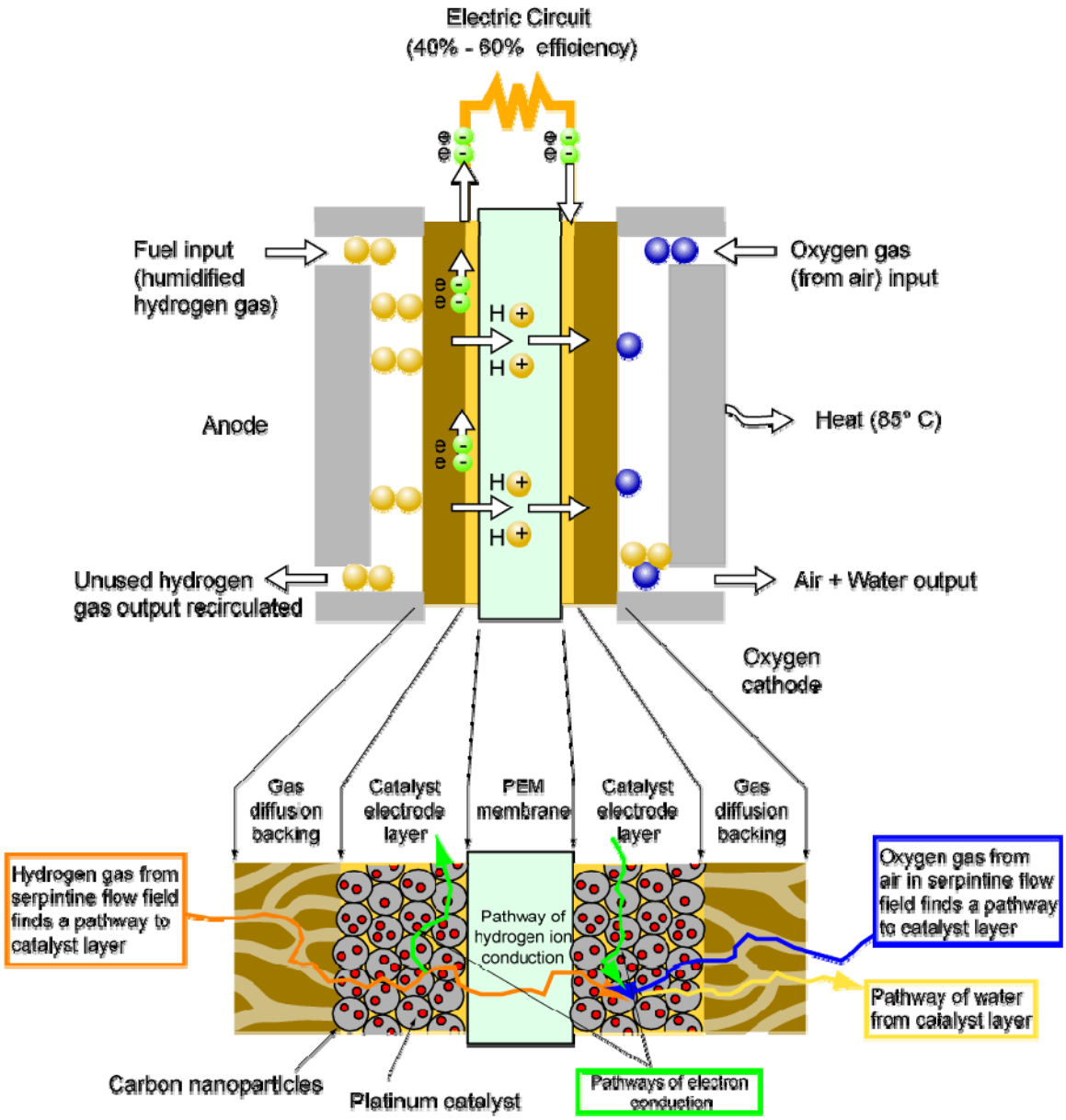

Figure 3: Schematic diagram of a proton exchange membrane fuel cell.

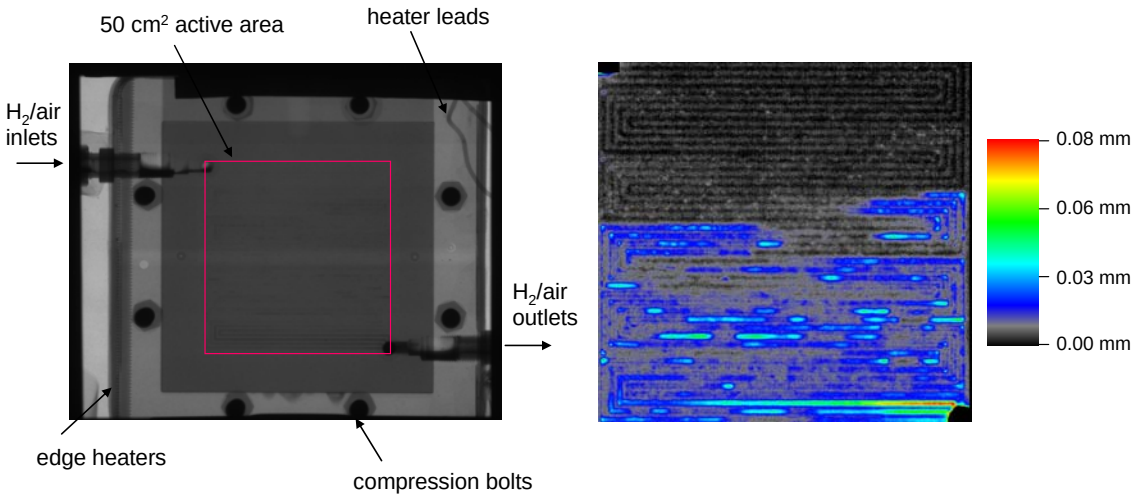

Figure 4: Neutron radiograph of a 50 cm^2 active area fuel cell and a false-color radiographa section of gas flow channels in an operating fuel cell. The color bar on the right indicates the water thickness in each pixel.

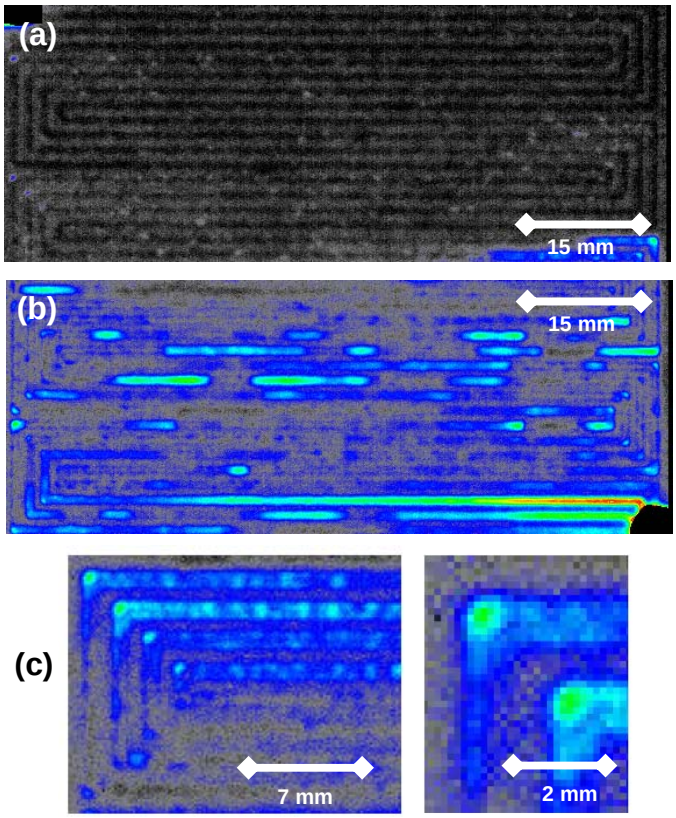

Figure 5: False color image of various areas of an operating cell showing (a) a relatively dry region where significant evaporation is occurring, (b) an area with more liquid water slugs in the gas flow channels, (c) a close-up of a channel bend, and (d) extreme close-up of two channel corners showing stagnation and resulting liquid water droplets in the bend of the corners.

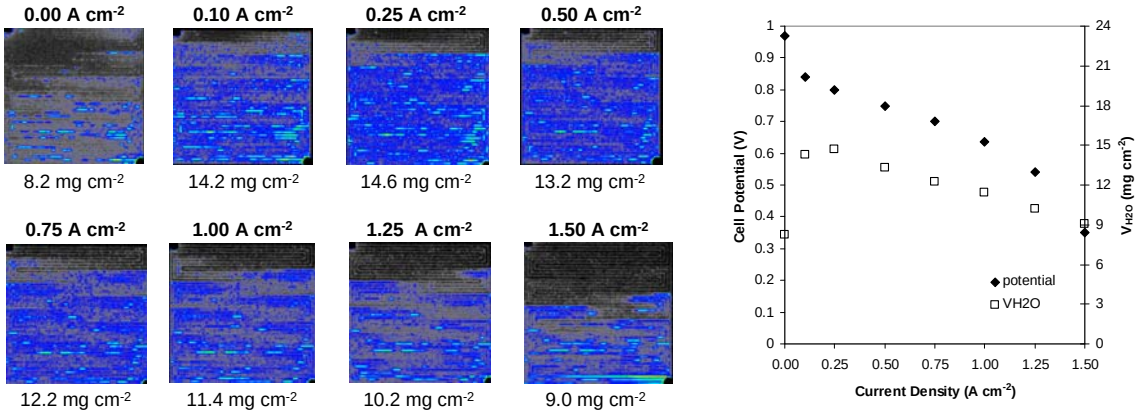

Figure 6: Neutron radiographs of a 50 cm^2 PEMFC operating at 80°C and a stoichiometric flow rate of 2 showing the effect of current density on liquid water content and distribution. Both gas inlets are in the upper left of the images and both gas outlets are in the lower right of the images. Gravity is pointing downward in the images.

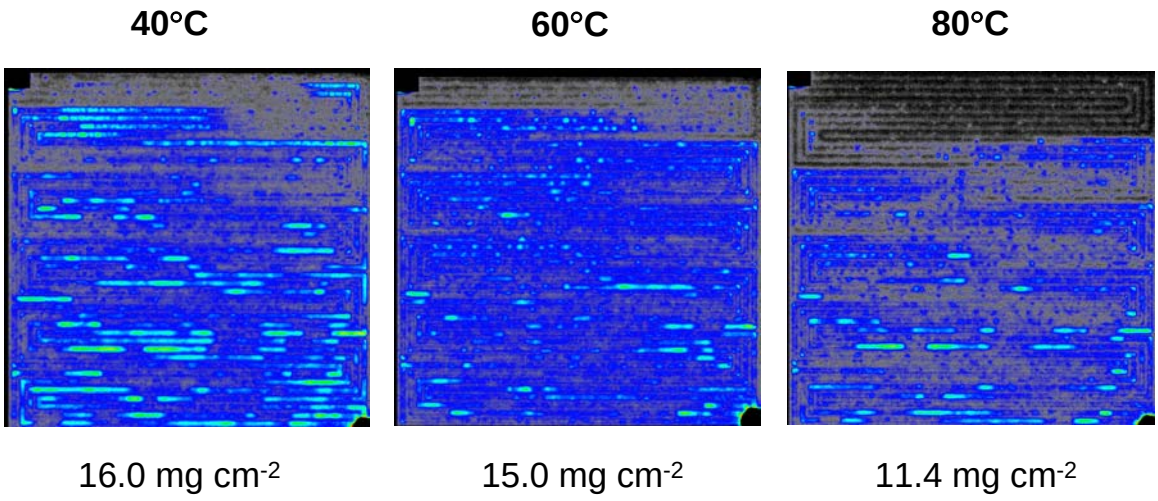

Figure 7: Liquid water content of 50 cm^2 operating fuel cells with a current density of 1 A cm^{-2} at different temperatures.

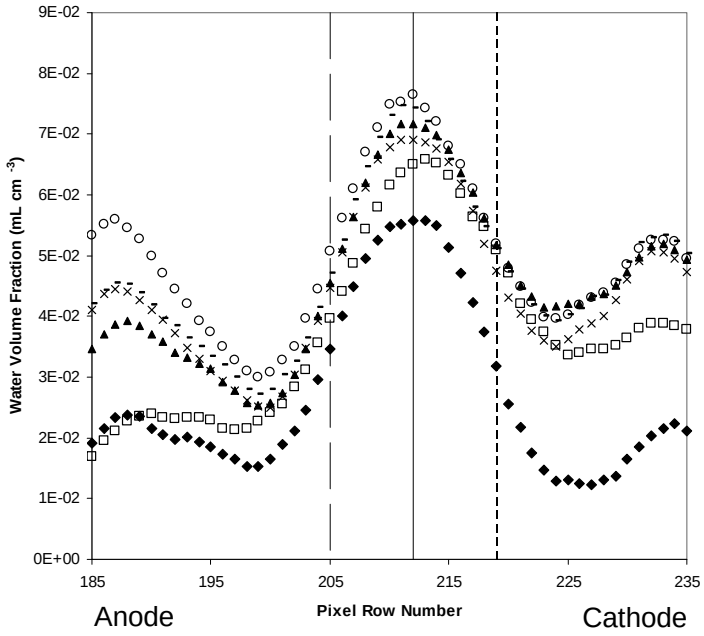

Figure 8: Detailed MEA cross-sectional water volume fraction for 60 °C cell temperature as a function of current density; (♦) 0.00 A cm^{-1}, (□) 0.10 A cm^{-1}, (▲) 0.50 A cm^{-1}, (-) 0.75 A cm^{-1}, (○) 1.00 A cm^{-1}, (x) 1.25 A cm^{-1}. Solid line demarks the center of the membrane, dashed lines demark the microporous layer/macroporous layer boundary from the image data.

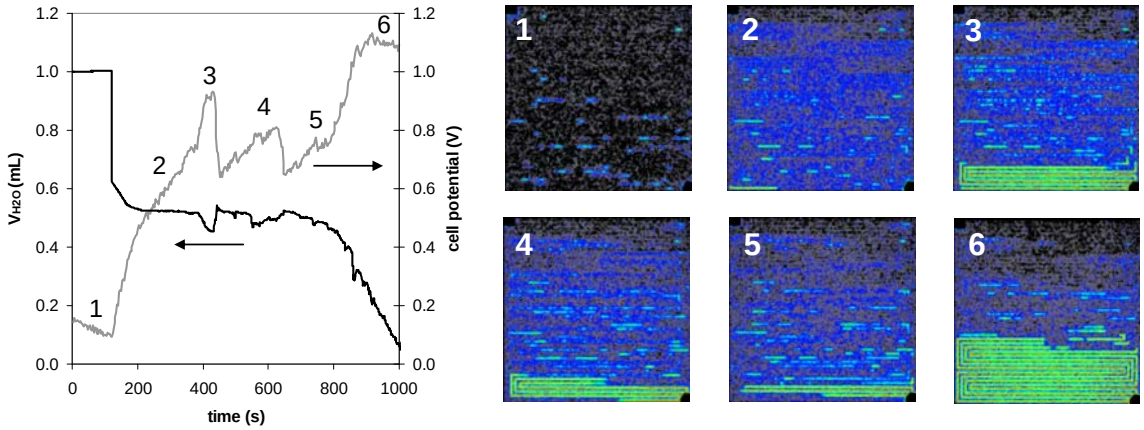

Figure 9: Time-resolved water build-up response of a fuel cell in response to a step-change in current density from open circuit to 1.5 A cm^{-2} at 60 °C and 4 stoichiometry gas flow.

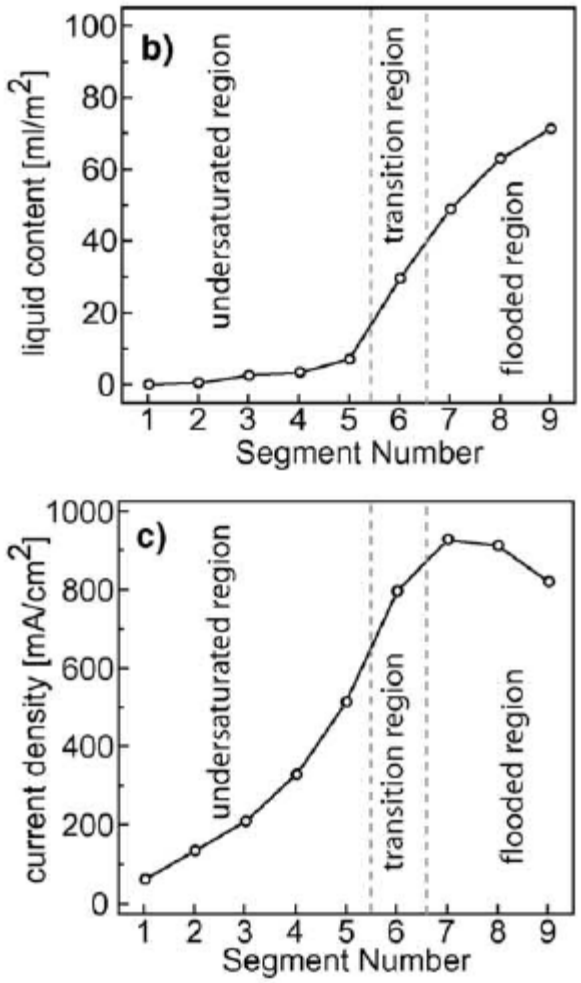

Figure 10: Liquid water profile and current density distribution from the inlet to the outlet of an operating 29.2 cm2 active area cell.[36]

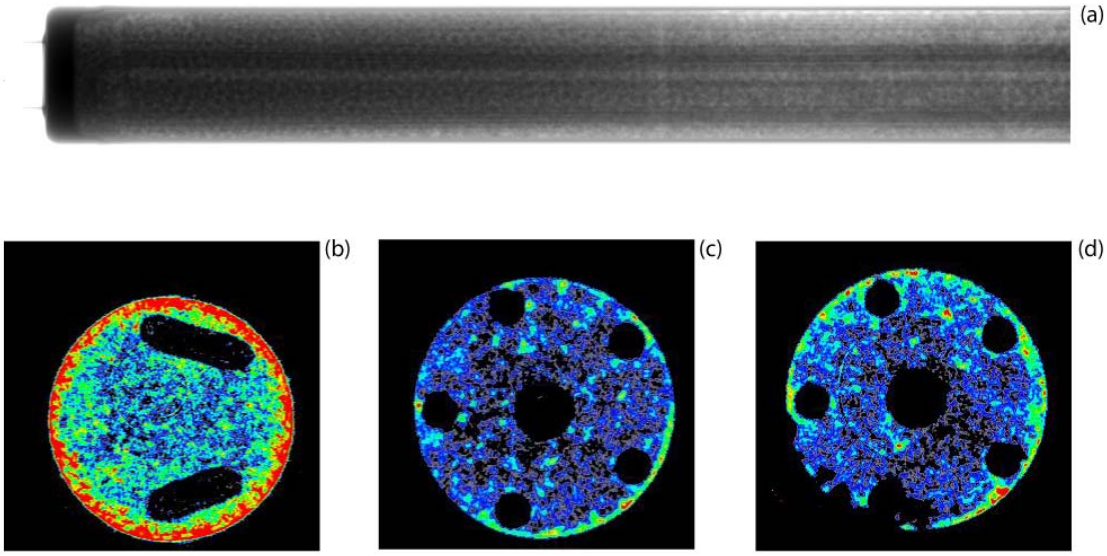

Figure 11: Images from a neutron tomogram of a hydrogen storage bed. (a) One normalized projection of the metal-hydride bed, wherein the porous structure of the aluminum foam and metal powder are visible. (b-d) Using "*in situ*" tomography, the hydrogen content can be directly obtained by subtracting the tomogram of the uncharged state from the charged state. Shown in (b-d) is the colorized hydrogen content obtained from this subtraction, for different slices through the bed, at different points along the bed length. In (b) this near the end of the bed and the internal heater bends visible as black oval regions. The hydrogen is seen to preferentially accumulate all the out circumference of the bed, where there is more effective heat exchange with the environment. In (c), the internal heater is visible as the five black circles along the outer circumference. The hollow gas inlet in the center is also black, indicating that there is insufficient sensitivity to see the attenuation due to the gas phase. The hydrogen still accumulates along the outer circumference, and is concentrated in pockets, not uniformly distributed. (d) A slice at the end of the imaged portion of the bed. The absence of hydrogen in the lower left of the bed is due to a lack of metal powder in this region.

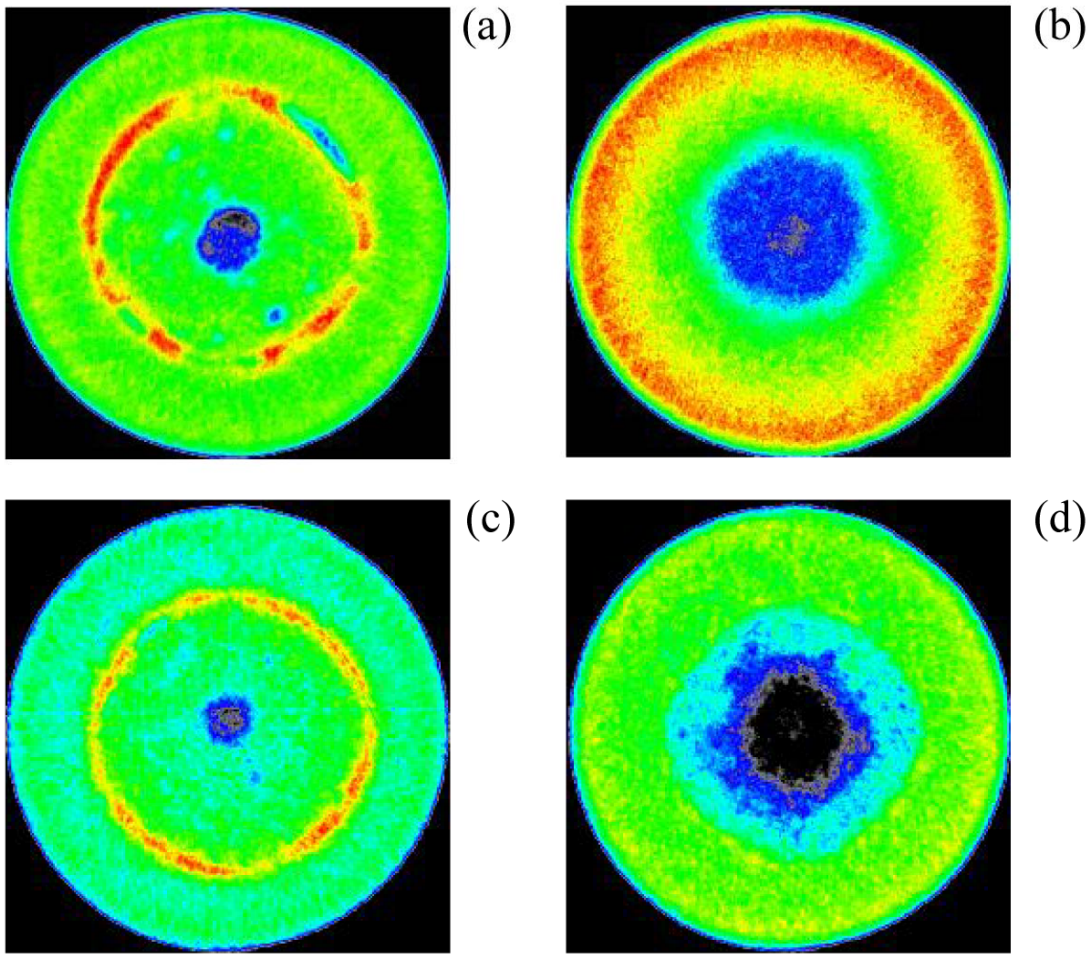

Figure 12: Comparison of the attenuation in an alkaline AA cell after operation at a constant current. For all images, black is low attenuation, red is high attenuation. (a) Fresh cell before operation at 50 mA (b) discharged cell after operation at 50 mA for 52.5 h. The electrolyte has an initially uniform distribution (green), and the separator is clearly visible. At the end of life, the electrolyte is concentrated at the outer circumference, and has been depleted from the separator. Further, the anode near the anode pin has little to no electrolyte. (c) Fresh cell before operation at a constant 1 A (d) discharged cell after operation at 1 A for about 70 min. In discharge at higher current, there is a clear change in the electrolyte concentration at the separator boundary, as opposed to the smooth transition in (b). Also, the region in the anode devoid of electrolyte (black) is significantly larger.